Finite-size criticality in fully connected spin models on superconducting quantum hardware

Michele Grossi [ORCID],[1,*] Oriel Kiss [ORCID],[1,2] Francesco De Luca [ORCID],[3] Carlo Zollo [ORCID],[3] Ian Gremese [ORCID],[3] and Antonio Mandarino [ORCID][4,†]

[1]*European Organization for Nuclear Research (CERN), 1211 Geneva, Switzerland*
[2]*Department of Particle and Nuclear Physics, University of Geneva, 1211 Geneva, Switzerland*
[3]*Department of Physics, University of Trieste, 34127 Trieste, Italy*
[4]*International Centre for Theory of Quantum Technologies, University of Gdańsk, 80-309 Gdańsk, Poland*

The emergence of a collective behavior in a many-body system is responsible for the quantum criticality separating different phases of matter. Interacting spin systems in a magnetic field offer a tantalizing opportunity to test different approaches to study quantum phase transitions. In this work, we exploit the new resources offered by quantum algorithms to detect the quantum critical behavior of fully connected spin-1/2 models. We define a suitable Hamiltonian depending on an internal anisotropy parameter γ that allows us to examine three paradigmatic examples of spin models, whose lattice is a fully connected graph. We propose a method based on variational algorithms run on superconducting transmon qubits to detect the critical behavior for systems of finite size. We evaluate the energy gap between the first excited state and the ground state, the magnetization along the easy axis of the system, and the spin-spin correlations. We finally report a discussion about the feasibility of scaling such approach on a real quantum device for a system having a dimension such that classical simulations start requiring significant resources.

I. INTRODUCTION

The abrupt change of the system properties during a phase transition has always paved the way to the advancement of our understanding of nature in both fundamental and applied aspects. The phase transition mechanism, in the limit of an infinite number of particle composing the system, has been successfully addressed within the formalism of the renormalization group [1,2]. Quantum phase transitions are the cornerstone of a great variety of ground-breaking theories ranging from the Higgs mechanism for mass generation in high-energy physics [3,4] to the superfluid and superconducting phase of matters in low-energy physics [5,6], and now their exploitation is getting attention. also in the context of quantum technologies [7,8].

Given a Hamiltonian $H(\vec{\lambda})$, describing a system constituted by N interacting particles, it exhibits a continuous (or second-order) quantum phase transition, whether in the limit $N \to \infty$, the gap between the energies of the ground state and the first excited state vanishes for a certain value of the internal parameters $\vec{\lambda}$. This value corresponds to the critical point of the model and, in contrast to any classical model, it can also exist for zero temperature [9,10]. Nevertheless, assuming a diverging number of particle is well motivated and substantiated. The relaxation of such assumption prompts the study of finite-size corrections to such transition [11,12] that can show unprecedented results [13–15]. With abuse of notation we write that a quantum phase transition occurs in a system with finite N, whenever for a value of $\vec{\lambda}$, a crossing between

the energies of the ground state and the first excited level is observed. This is in contrast to what one would expect by a semiclassical approach in which the finite size is responsible for suppressing the symmetry-breaking mechanism associated with the second-order phase transition [11,16]. Criticality of quantum system requires an exponential number of degrees of freedom that makes the problem quickly intractable. The advancement of machine-learning techniques has been of paramount importance for the determination of macroscopic phases of matter and efficient quantum-state representation.

With the advent of quantum techniques in machine learning, phase diagrams of different systems have been obtained, such as a cluster Ising or the Bose-Hubbard model at zero temperature. The former uses a supervised learning approach where the states are classified according to classical labels using a quantum convolutional neural network [17–19], while the latter discovers the phases in an unsupervised way using anomaly detection [20]. The intersection between machine learning and quantum techniques applied to physical systems is rapidly increasing; not only is obtaining information about critical point of a system pursued but also general dynamical simulations are important testbeds. In Ref. [21] the authors rigorously analyze the requirements of an algorithm in terms of training data and define generalization bounds for their effective execution on current quantum devices. For an overview of the state of the art and future perspectives for quantum simulation, looking at possible quantum advantage in specific applications we refer to Ref. [22].

We consider the Lipkin-Meshkov-Glick (LMG) model, a fermionic model that served as a testbed for many-body approximations in different fields [23–25]. Due to the possibility of mapping this model into an N spin-1/2 system, we will study its criticality with current quantum computation

*michele.grossi@cern.ch
†antonio.mandarino@ug.edu.pl

techniques on real noisy-intermediate-scale quantum (NISQ) devices [26,27].

Here we propose a way to study the finite-size critical behavior of the system with the freshly introduced methods of quantum machine learning. Our motivation is threefold. First, very few examples of such methods have been used to study magnetic systems [28]. Second, the finite size criticality with regard to this model is of interest to the molecular magnetism community [29]. Last, and a bit ambitiously, we would like to pave the way to a feasible application of the now-available NISQ hardware as a tool to simulate physics with (quantum) computers. In fact, before addressing more complex magnetic systems, we have chosen as a testbed a magnetic model that, due to its symmetries, served to validate geometrical methods developed in the framework of quantum information [30–32] as signature of quantum phase transitions. However, the class of models that can be studied are not so trivially integrable to be considered as a mere academic exercise.

A simplified version of the spin model that we consider has been tackled in recent papers [33–36] for system up to four spins and the analysis is carried on noiseless simulators. This allows us to contribute to the validation of a *heuristic* approach such as the variational quantum eigensolver (VQE) [37,38] in the challenging research field of statistical physics of finite-size models on a lattice.

The remainder of this paper is structured as follows: In Sec. II we provide a short but comprehensive introduction to the VQE technique, and then we focus on the definition of the wave-function ansatz in terms of design and trainability of quantum circuits and provide an overview of the adopted error mitigation techniques, with ad hoc consideration for the specific Hamiltonian. After introducing all the tools, we terminate the section with the definition of the LMG Hamiltonian of our critical system. In Sec. III, we substantiate our approach showing simulated results obtained under ideal condition with quantum simulator as well as evidences collected on real quantum device. In Sec. IV, we provide a numerical interpretation and analytical derivation of higher-order excited states for the LMG model, as well as their realisation with the variational algorithm. Finally, in Sec. V, we summarize the outcomes of this work, discussing the quality of the results with an estimation about the actual feasibility of studying proposed models, like on NISQ devices.

II. METHODS

In this section, before introducing the Hamiltonian of an LMG critical system and its behavior in the thermodynamic limit, we review the quantum computational techniques that we employ to assess the critical behavior of the system.

A. Variational quantum eigensolver

The VQE, proposed by Peruzzo *et al.* [37], is a variational quantum algorithm [39] used to find the ground state of a Hamiltonian H by using the Rayleigh-Ritz variational principle. This variational method has been widely applied in quantum chemistry [40–43], nuclear physics [44–46], and spin systems [28,33–36,47,48].

Concretely, a parametrized wave function $|\psi(\theta)\rangle$ [49] is prepared on a quantum computer and its parameters updated to minimize the energy,

$$E_0 \leqslant \frac{\langle \psi(\theta)|H|\psi(\theta)\rangle}{\langle \psi(\theta)|\psi(\theta)\rangle}, \qquad (1)$$

where the normalization factor at the denominator can be dropped if the wave function is normalized.

The design of the wave-function ansatz is of importance for the trainability and accuracy of the results and is an active area of research. Some systems, typically written in the second quantisation formalism, allow physically motivated ansätze, for instance based on unitary coupled cluster [40,45,46,50,51]. In this setting the related quantum circuits are usually deep, require an increased connectivity, and are therefore difficult to implement on near term quantum devices. On the other hand, hardware efficient ansatz (HEA) [41] are tailored to the device and are consequently shallow enough to minimize the effects of noise and decoherence. Despite working with shallow circuit, in general HEA may suffer from scalability issues due to the increasing number of parameters to optimize, leading to untrainability issues, namely barren plateau [52]. An alternative direction to optimize the choice of the ansätze is the possibility of exploiting symmetries in the system. As recently proposed in Ref. [53] it is possible to work with equivariant ansätze which might mitigate the barren plateau problem. However, as underlined by the authors, there a trade-off always exists between the equivariance and expressivity of the parametric circuit.

More recently, the ADAPT-VQE [54], which builds the ansatz by iteratively adding a term from an operator pool bringing the best improvement, has been proposed as a way to build optimal circuits. Even if the picking action can be implemented in a parallel fashion, it can be expensive for current devices, time- and resources-wise. Consequently, we will focus on fixed hardware-efficient ansätze, which are constructed with single qubit rotations around the *y*-axis, and CNOT interactions with linear connectivity.

The VQE can be extended to compute excited states as well. The method adopted here is the one proposed by Higgott *et al.* [55], called *variational quantum deflation* (VQD), which first computes the ground state and then looks for the state minimizing the energy while being orthogonal to the, previously determined, ground state. This procedure can be generalize for the *k*th excited state in an iterative fashion. In practice, the following loss function is minimized:

$$F(\theta_k) = \langle \psi(\theta_k)|H|\psi(\theta_k)\rangle + \sum_{i=0}^{k-1} \beta_i \langle \psi(\theta_k)|\psi(\theta_i)\rangle, \qquad (2)$$

where we assume, for simplicity, that the states are normalized. The wave function $|\psi(\theta_i)\rangle$ corresponds to the *i*th excited state and β_i hyperparameters to be tuned. It has been shown [55] that β_i has to be greater than the energy gap between the states i and $i+1$ to ensure that the wave function converges to the correct excited state. Additional techniques, based on the quantum equation of motion [56], using a discriminator [57], or constraining the ansatz around the state of interest [58] have been proposed in the literature but will not be considered here.
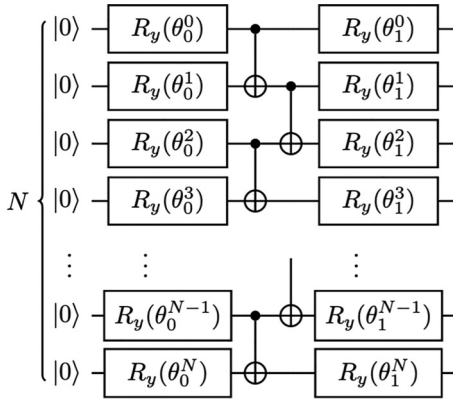
FIG. 1. Representation of the chosen ansatz to design the parametric function $\psi(\theta)$, namely the Hardware efficient ansatz, composed of $R_y(\theta)$ rotations and CNOTs between neighboring qubits executed in parallel. We sketch here a single layer of the circuit, corresponding to $D = 1$, where higher values of D correspond to sequential repetitions of such a circuit.

B. Ansatz

We use a simple hardware efficient ansatz [41], which can be run on NISQ devices without an overhead due to circuit transpilation. For instance, we use D repetitions of a layer consisting of free rotations around the y axis $R_y(\theta) = e^{-i\theta\sigma_y/2}$, where σ_y is the y Pauli matrix, CNOT gates with linear connectivity, and a final rotation layer before the measurements. Since the depth of the circuits grows as $\mathcal{O}(N)$ due to the linear entanglement, this ansatz fails on hardware when performing error mitigation based on noise scaling. We therefore adapt the ansatz to grow as $\mathcal{O}(1)$ by applying the CNOT gates in parallel on the two following groups of qubits:

$$\{(i, i+1) \ \text{for } i \text{ even}\},$$
$$\{(i, i+1) \ \text{for } i \text{ odd}\},$$

thus considerably reducing the depth of the circuits. We observe a small decrease in the accuracy on the simulator compared to the linear entanglement scheme but an increase on the hardware due to the depth's reduction. We choose the minimal case $D = 1$, as depicted in Fig. 1, when running on quantum hardware, while pushing for maximal performance on the simulator by allowing larger D.

C. Error mitigation

Error mitigation methods are used to diminish the effect of the hardware noise on the results. Unlike error correction, these strategies are used in the postprocessing steps on the raw data. Two complementary techniques, measurement error mitigation (MEM) and zero noise extrapolation (ZNE), are used to mitigate the readout and two-qubit gate errors, respectively.

For MEM, we follow Nation *et al.* [59] and individually invert the error matrices

$$M^k = \begin{bmatrix} P_{0,0}^{(k)} & P_{0,1}^{(k)} \\ P_{1,0}^{(k)} & P_{1,1}^{(k)} \end{bmatrix} \tag{3}$$

and used them to calibrate the samples. Here $P_{i,j}^{(k)}$ is the probability of the kth qubit to be in state $j \in \{0, 1\}$ while measured in state $i \in \{0, 1\}$. The probabilities of measuring 0 or 1,

$$\vec{S}^k = \begin{pmatrix} P_0 \\ P_1 \end{pmatrix} \tag{4}$$

obtained by measuring the kth qubit, are corrected as follows:

$$\vec{S}_{\text{corrected}}^k = (M^k)^{-1}\vec{S}^k. \tag{5}$$

While this only corrects uncorrelated readout errors, it is argued in Ref. [59] that they are the predominant ones. Moreover, this strategy can be scaled for an arbitrary number of qubits and only has a $\mathcal{O}(1)$ overhead in the number of circuit execution. In the ZNE [60,61] scheme, the CNOT noise is artificially stretched and the results are then extrapolated to the noiseless regime. More precisely, the energy is estimated multiples time for different scaling factor $k \in \{1, 2\}$, and then a fit is performed to extrapolate up to the $k = 0$ value. In practice, the noise is stretched by replacing every CNOT in the circuit by $2k - 1$ CNOT gates. The $2k - 2$ additional CNOTs cancel each other, leaving the circuit unchanged. However, by adding barriers between them, preventing the CNOTs from being canceled in the transpilation phase, the noise is artificially stretched. Richardson [62] originally used a linear fit for the extrapolation; however, the considerable effect of the noise in NISQ devices increases the risk of overshooting. Consequently, an exponential fit $f(x) = ae^{bx}$ is instead used, where a and $b \in \mathbb{R}$ are fitted to the energies E using least-squares regression. To improve the results, E is scaled before the fit

$$E \mapsto \frac{E - s}{s} \tag{6}$$

and scaled back afterwards, with s being an estimate of the exact energy. In ZNE the scaling of sampling required could also be exponential, at least in some cases [63]. Of course this is just a theoretical upper bound in measurement but in practice we use a scalable MEM method which requires only two circuits as a sufficient quantity to mitigate the noise.

It is important to make sure that the total runtime of the noise-scaled circuits does not exceed the coherence time of the device, which would destroy any useful information. For instance, we only considered $k = 1$ and $k = 2$, since for higher k the results were no longer reliable. Also the ansatz definition plays an important role, as described in Sec. II B. With the construction of Fig. 1, the CNOT gates can be run in parallel, thus shortening the runtime significantly. This can be done using additional qubits available on the device to run all the noise-scaled circuits in parallel, reducing the total number of circuit execution; however, for sake of meticulousness one can note that in principle this strategy might result in additional cross-talk, even if, looking at IBM current hexagon topology, one can really minimize this effect.

D. The Lipkin-Meshkov-Glick model

The LMG model was introduced in Refs. [23–25] to describe a system of N fermions whose state space is made of two degenerate shells with two fixed energy levels. Each shell has degeneracy N and can accommodate all of the N particles, thus resulting in a total of a 2^N-dimensional state space. Due

to the symmetry of the Hamiltonian with the total spin, the low-energy states are in the subspace of maximum spin, which has a dimension that scales linearly with N. However, to substantiate our approach we do not consider only the maximum spin sector of the Hamiltonian, but we use the VQE on the full space as outlined in Sec. II A. Via a Jordan-Wigner transformation [64], the LMG model can be mapped into a system of interacting spins. Moreover, in the thermodynamic limit $N \to \infty$, it is solvable via a two-boson Holstein-Primakoff transformation [65]. This peculiarity made it one of the most used models to understand many problems of interest in physics, from nuclear to condensed-matter physics.

Considering that we will study our model on qubit-based quantum computers, it is natural and convenient to use the following expression for the LMG Hamiltonian:

$$ H = -\frac{1}{N} \sum_{i<j}^{N} \sigma_x^i \sigma_x^j + \gamma \sigma_y^i \sigma_y^j - B \sum_{i=1}^{N} \sigma_z^i. \tag{7} $$

This Hamiltonian describes a system of N spins in a fully connected planar graph, immersed in a transverse magnetic field B. The first sum in Eq. (7) accounts for an anisotropic interaction in the x-y plane that couples each spin with all the other ones with the same strength, an archetype and exemplary version of any long-range interaction. Different coupling strengths along the two planar directions are taken into account via the anisotropy parameter $0 \leqslant \gamma \leqslant 1$. From a physical perspective, this type of Hamiltonian has been implemented on various platforms [66–69] to design feasible quantum technologies applications [70–75].

The system is known to be critical and shows, in the thermodynamic limit, a second-order phase transition between a broken-symmetry (disordered) phase for $B < 1$ and an ordered phase for $B \geqslant 1$, with a critical value of the external magnetic field $B = B_c = 1$. Usually, the Lipkin model is used to denote a limiting and easily diagonalizable case of the LMG model [76]. Introducing the set of collective-spin operators $S_\alpha = \frac{1}{2} \sum_{i=1}^{N} \sigma_\alpha^i$, and setting $\gamma = 1$ in Eq. (7), we have:

$$ H = -\frac{2}{N}\left(\mathbf{S}^2 - S_z^2\right) - 2BS_z. \tag{8} $$

The Hamiltonian in Eq. (8) is diagonal on the Dicke basis $|j, m\rangle$ formed by the simultaneous eigenvectors of $\mathbf{S}^2|j, m\rangle = j(j+1)|j, m\rangle$ and $S_z|j, m\rangle = m|j, m\rangle$. Due to the fact that the interaction term commutes with the free-energy term, the Lipkin model with $\gamma = 1$ belongs to a different universality class of the general model described by the Hamiltonian in Eq. (8); see Ref. [65]. In particular, it has been shown to belong to the same class of the super-radiant Dicke model [77]. Within our formalism, we can also address the criticality of the fully connected Ising model imposing $\gamma = 0$. This model presents, in the thermodynamical limit, a quantum phase transition due the spontaneous breaking of the $\mathbb{Z}_2$ symmetry [78].

The phase diagram of this model at zero temperature was derived in Ref. [79], thanks to a two-boson Schwinger boson realization of the $SU(1, 1)$ Richardson-Gaudin integrable models. However, classifying phase transitions in systems having finite number of elements is a challenging and an open problem. In particular, in the quantum domain, the issue relating to the scaling of the Hilbert space size, such us

the exponentially growing size of the Hilbert space for the considered systems, impacts strongly the performance of classical techniques.

We will study the precursors of the quantum phase transition for the finite-size LMG model via quantum computational techniques. With abuse of notation, we will call the values of the magnetic field B and of the anisotropy γ, for which the ground state and the first excited state of the system are degenerate, critical values.

The adopted strategy can be easily extended to other critical systems, but the choice of the LMG model to test our approach is driven by two reasons. On one side, the model is of interest for several communities and it has been used to test many-body approximations [65,80]. The expression in Eq. (7), in terms of Pauli operators, makes the implementation on a superconducting quantum processor quite straightforward and requires less physical resources compared with its fermionic formulation. On the other side, the model has some peculiarities, namely anisotropy and long-range interaction, that makes it a nontrivial model to assess quantum criticality at finite size.

III. RESULTS

This section presents the numerical results obtained in this work. We remark that a truly QPT is related to a singular behavior of the energy spectrum and the consequent nonanalyticity of several observable quantities such as the magnetization. For systems of finite size a critical behavior occurs when the ground-state energy has a level-crossing, viz., there is an interchange of the ground-state level and the first excited state at a critical point. This reflects in a null energy gap at the critical point and in a nonanalytic behavior of the mean magnetization along the model easy axis. Section III A contains the ground- and first-excited-state energy and magnetization for $N = 4, 5, 6$ spins and different values of γ and B obtained on state vector simulations and we analyze their behavior in the anisotropic and isotropic case. Section III B shows the ground-state energy and magnetization for $N = 5$ spins, $\gamma = 0.49$, and different values of B computed on superconducting transmon qubits and comments on the scalability of the VQE in the near term. We refer to Appendix for a detailed explanation about different simulation backends and variational circuit optimizers.

A. Noiseless VQE simulations

For a small number of spins N, the classical approach of the diagonalization of H is straightforward. Defining the spectrum of the Hamiltonian $H|\psi_n\rangle = E_n|\psi_n\rangle$ with $n = \{0, \ldots, 2^{N-1}\}$, multiple crossing points between the energies of the ground and the first excited state (E_{GS} and E_{1st}, respectively) are found for the following critical values:

$$ B_C^k = \frac{N-k}{N}\sqrt{\gamma}, \tag{9} $$

for a fixed γ, $k \leqslant N$, and odd [80]. Hence, the ground-state energy can be recast in $N/2 + 1$ *phases* if N is even or in $(N - 1)/2 + 1$ otherwise. Introducing the ground-state magnetization along the model easy axis $\langle S_z \rangle = \langle \psi_0(B, \gamma)|S_z|\psi_0(B, \gamma)\rangle$,

we can observe that for any nonanalytic point $\lim_{B \to B_C^{k-}} \langle S_z \rangle \neq \lim_{B \to B_C^{k+}} \langle S_z \rangle \, \forall B_C^{(k)}$ holds. In the following, we will denote $|\psi_0\rangle \equiv |\psi_{GS}\rangle$ and $|\psi_1\rangle \equiv |\psi_{1st}\rangle$.

We use state vector simulations as a theoretical tool to explore more-complex ansatz and increase the performance as much as possible. We choose the depth of the ansatz as a function of the system size, namely $D = N$. This differs from the results obtained on real hardware, as explained in Sec. II B. The training is performed with the SLSQP optimizer [81] with 2000 maximum iterations. Adiabatic computing is applied to speed up the calculations and improve the accuracy, following the recommendation of Harwood *et al.* [82]. The excited states are found using a VQD-like algorithm. Using the state vector given by the solution of the Hamiltonian it is possible to redefine a new effective Hamiltonian,

$$H' = H + \beta_0 |\psi_{GS}\rangle\langle\psi_{GS}|. \tag{10}$$

When the superposition between $|\psi_{1st}\rangle$ found by using VQE on H' and $|\psi_{GS}\rangle$ is small the loss function associated to this Hamiltonian reduces to Eq. (2) with $k = 1$. We found this to be true every time the β_0 is set greater than the energy gap between the ground and first excited state, as specified in Sec. II A. Knowing that transitions happen for $B = B_C^k$, see Eq. (9), we choose five points between the transition points and the chosen bounds. Starting from the upper bound, where the energy gap is wider, the ground-state energy and the first excited energy are evaluated using random initial parameters. For each point in the interval, in decreasing order, the optimal point found in the previous step are chosen as initial parameters. Moreover, for the next interval, the optimal parameters for the ground state are used as the initial point as well as for the first excited state. This technique significantly speeds up the simulation, improves the quality of the results, and allows us to compute the energies for systems up to $N = 10$ spins, using state vector simulations.

Figure 2 shows the ground- and first-excited-state energy for an LMG Hamiltonian with $N = 4$ spins for the specific value of $\gamma = 0.81$, as a function of the magnetic field B. The VQE is compared to the exact diagonalization (black solid lines), while the VQE points are obtained using state vector simulation (crosses) as well as shoots-based probabilistic output without hardware noise contribution (filled squares and circles). We will refer to the second case as to QASM simulation, intending noise free simulation with finite statistics. Another figure of merit to assess a quantum phase transition for finite-size systems is the energy difference between the first excited state and the ground state, namely $E_{1st} - E_{GS}$ (to which we will refer to as the gap, for shorthand of notation). The gap as a function of the magnetic field is shown in Fig. 3 for $N = 5$ spins and two values of γ, $\gamma = 0.36, 0.81$. Even if they are far from the extreme values $0, 1$ they already underline a difference in the behavior, at least for $B < 0.6$. Similar considerations hold as a function of the system size, shown in Fig. 4 for $N = 4, 5, 6$ with $\gamma = 0.44$. In both cases, the energy gap rapidly explodes after $B \geqslant 0.6$.

Finally, we consider the extreme cases of the fully connected Ising model and the Lipkin-Dicke model for $\gamma = \{0, 1\}$ respectively. We report our results in Fig. 5, together with an intermediate γ value of 0.49, where the system size is fixed to
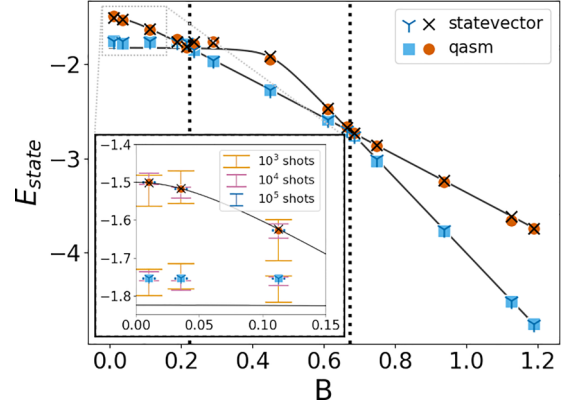

FIG. 2. We report the energies of the ground state E_{GS} and first excited one E_{1st} of the Hamiltonian in Eq. (7) for $N = 4$ and for value of the anisotropy parameter $\gamma = 0.81$ as a function of the magnetic field B. Solid lines represent the values obtained via exact classical diagonalization, while discrete points are the results obtained via VQE. The results for E_{GS} are marked in light blue with tri-down markers (state vector simulation) and filled squares (QASM noiseless simulation), while results for E_{1st} are in orange with crosses marking the state vector simulation and filled circles the QASM noiseless outputs. Vertical dotted lines show crossing points for values given in Eq. (9). The inset makes it possible to better appreciate the accuracy of energy estimates as a function of the number of shoots, where the error bar correspond to one standard deviation.

$N = 5$. The energy gap between the first excited state and the ground state is shown in Fig. 5(a), while the correlation function along the x axis $\langle S_x^2 \rangle$ in Fig. 5(b) and the magnetization along the longitudinal direction of the magnetic field $\langle S_z \rangle$ in Fig. 5(c). We have decided to plot the correlation function $\langle S_x^2 \rangle$ because, due to the spin-flip simmetry of the Hamiltonian in
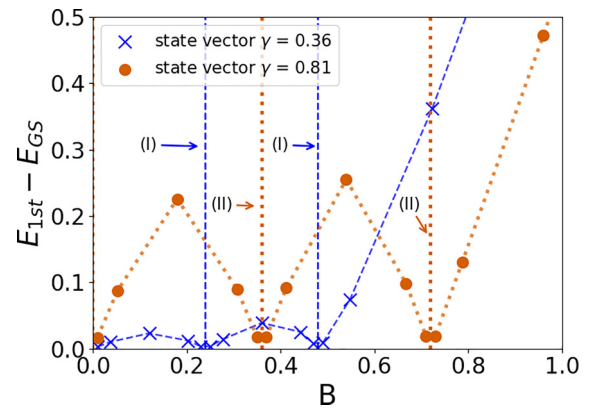

FIG. 3. We plot the difference between the energy of the first-excited-state E_{1st} and the ground-state energy E_{GS} as a function of the tuning field B. The results are shown for a system with $N = 5$ lattice sites, focusing on different values of the anisotropy parameter $\gamma = 0.36, 0.81$. The results obtained via VQE are marked by blue crosses ($\gamma = 0.36$) and orange dots ($\gamma = 0.81$). The blue dashed line ($\gamma = 0.36$) and the orange dotted line ($\gamma = 0.81$) represent the exact diagonalization values of $E_{1st} - E_{GS}$. Vertical lines correspond to values of the critical magnetic field such that Eq. (9) holds, where the (I) refers to $\gamma = 0.36$ and (II) to $\gamma = 0.81$.

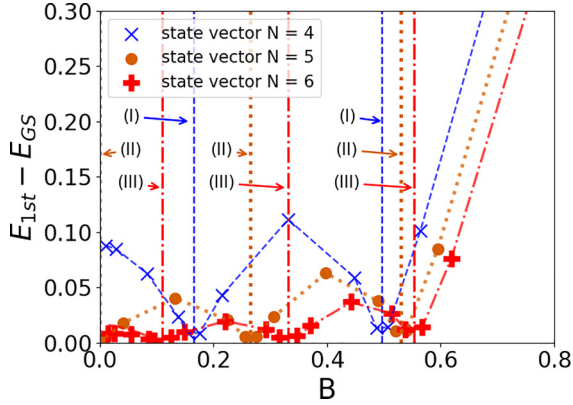FIG. 4. We report the energy difference $E_{1st} - E_{GS}$ as a function of the magnetic field B. The results are computed at $\gamma = 0.44$ for different lattice sizes $N = 4$ (blue), $N = 5$ (orange), and $N = 6$ (red). The results obtained via VQE are represented by a blue cross ($N = 4$), an orange dot ($N = 5$), and a red plus ($N = 6$), while the blue dashed line ($N = 4$), the orange dotted line ($N = 5$), and a red dot-dashed line ($N = 6$) represent the values obtained by exact diagonalization of the Hamiltonian H. The vertical lines correspond to the values of the magnetic field for which by we observe a crossing points between the two lowest state energies [see Eq. (9)]; they are labeled with (I) for $N = 4$, (II) for $N = 5$, and (III) for $N = 6$ sites.

Eq. (7), the mean value of the magnetization along the plane perpendicular the magnetic field is zero (see Ref. [65].) We observe the oscillatory trend of the energy gap for $\gamma = 1$ as opposed to the monotonic trend of the isotropic case ($\gamma = 0$). A completely different behavior can be appreciated also for the two magnetization observable, where the anisotropic model is characterized by a stepwise trend as opposed to the continuous one for $\gamma = 0$, signaling how the three models in the thermodynamic limit belong to distinct universality classes.

B. Runs on the real devices

1. Experimental device

The quantum device used in this work consists of 27 fixed-frequency transmons qubits, with fundamental transition frequencies of approximately 5 GHz and anharmonicities of -340 MHz, with the same topology as displayed in Fig. 6. Microwave pulses are used for single-qubit gates and cross-resonance interaction [84] for two-qubit gates. The experiments took place over one month, but each different computation took place over a span of 5 h, without intermediate calibration, with the use of Qiskit Runtime. The median qubit lifetime T_1 of the qubits is 121 and 129 μs, the median coherence time T_2 is 90 and 135 μs, and the median readout and CNOT error is 0.014 and 0.045, respectively. The SABRE [85] algorithm is used for the transpilation to the quantum hardware.

2. Small system size

We begin by computing the ground-state energy of a system with $N = 5$ spins and $\gamma = 0.49$ for different values of the magnetic field B. We use the hardware efficient

ansatz with $D = 1$ repetition, as shown in Fig. 1. As a warm initialization, the ansatz is first trained on the noiseless simulator, and the optimal parameters are used as an educated guess for the initial parameters. The training is composed of a maximum 100 steps, or until convergence, with the simultaneous perturbation stochastic approximation (SPSA) [86] optimizer using a learning rate of 0.005 for the first 30 steps and 0.001 afterwards, using 8092 shots. The graphs are obtained with 32 000 shots and statistics are collected from five distinct runs. Measurement error mitigation and zero noise extrapolation are performed to enhance the results, which are shown in Fig. 7. Solid lines correspond to the exact diagonalization, the black dots to the noiseless QASM simulation with 32 000 shots, the blue crosses to the raw results from the quantum device, and the red ones to the mitigated energies. The error bars correspond to the 99.5% confidence interval. The inset shows the effect of different error mitigation tuning on a specific point. The $k = 1$ point corresponds to the original circuit while $k = 2$ to the dilated case, where every CNOT is replaced with three CNOTs. The cross shows a scaled exponential fit while the triangle a linear one. As explained in Sec. II C, the linear fit overshoots the true ground-state energy, while this is not the case for the scaled exponential fit.

We observe that the ground-state energy is reproduced with less than 1% error ratio everywhere, suggesting that the quality of current devices is good enough for such tasks. However, the computed magnetization observables are not equally accurate. The explanation is twofold: First, we observe that the noiseless simulations are also less precise than the energy calculations, more particularly for $\langle S_x^2 \rangle$ at large magnetic field. This is essentially caused by the ansatz which is too shallow to represent the true ground state but instead is only a good approximation with similar energy. But more importantly, there is a discrepancy between the noiseless and real hardware results, which is due to overfitting to the hardware noise. For the ground-state calculation the noise is adapted to get to the GS, according to the real condition, which includes the presence of noise, and this is why we refer to this as an overfitting behavior. By doing so, we get closer to the true energy but drift from the true ground state. The approximation in computing the correct ground state is amplified when $\langle S_x^2 \rangle$ and $\langle S_z \rangle$ are computed shifting uniformly the curve.

3. Discussion on large system size

Finally, we tried to extend the reach of VQE to sizes where simulations are unavailable due to the exponential scaling of the Hilbert space. Even if density-matrix renormalization group [87] techniques are able to compute the ground-state energy for a large number of spins ($\sim 10^2$), we choose $N = 20$ since it is out of reach, in terms of simulation time, for our availability. This problem is more interesting than the previous case since we are unable to start from a set of previously trained parameters. In addition, these calculations are also more challenging for current devices for the following reasons. Gradient-free optimizers, such as SPSA, require small amounts of circuit executions to estimate the gradient. Yet, since they rely on finite-difference techniques, the gradient is strongly affected by the noise and can lead to erratic paths in the optimization landscape. On the other hand, analyti-
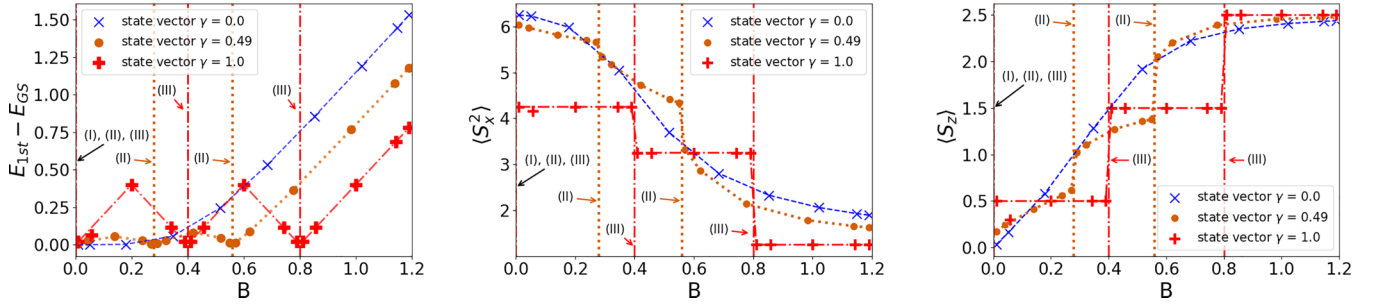
FIG. 5. We report the three relevant quantities to detect the criticality in a fully connected spin system. In (a) we show the energy gap $E_{1st} - E_{GS}$. In (b) we plot the correlation function $\langle S_x^2 \rangle$ and in (c) the mean magnetization along the direction of the magnetic field $\langle S_z \rangle$. The results are shown for $N = 5$ spins for particular values of the anisotropy identifying different classes of models $\gamma = 0$ (fully connected Ising model), $\gamma = 0.49$ (LMG model), and $\gamma = 1$ (Lipkin-Dicke model). In all the three plots, the results obtained via the quantum variational algorithm are represented by blue crosses ($\gamma = 0$), orange dots ($\gamma = 0.49$), and red plusses ($\gamma = 1$) and the benchmarking is given by the corresponding exact diagonalization values, shown as a blue dashed line ($\gamma = 0$), an orange dotted line ($\gamma = 0.49$), and a red dot-dashed line ($\gamma = 1$). The results are in agreement with the critical values in Eq. (9) and such values are reported as vertical lines [(I) denotes the only trivial value for $\gamma = 0$, (II) denotes critical values for $\gamma = 0.49$, and (III) denotes critical values for $\gamma = 1$].

cal gradients provided by the parameter-shift rule [88] are more reliable but also more expensive to compute, since they require $2 \cdot d$ circuit executions, where d is the number of parameters ($d = 40$ in this case). Accordingly, we estimate more than 1 h runtime per optimization step, accounting for error mitigation techniques, e.g., ZNE and MEM, which is more than what we can reasonably obtain from on a shared device and without running into further recalibration problems [63,89]. This is one of the main reasons an innovative integrated architecture of a quantum and classic computer like the one proposed by IBM with Qiskit Runtime would strongly reduce the computation time.

IV. HIGHER EXCITED STATES

The VQE can be used to compute the energies of the second and third excited states as well. Figures 8 and 9 show the seven lowest energy eigenvalues for a system of $N = 4$ spins as a function of the magnetic field B at two different interaction configurations $\gamma = \{1, 0.67\}$, respectively. The
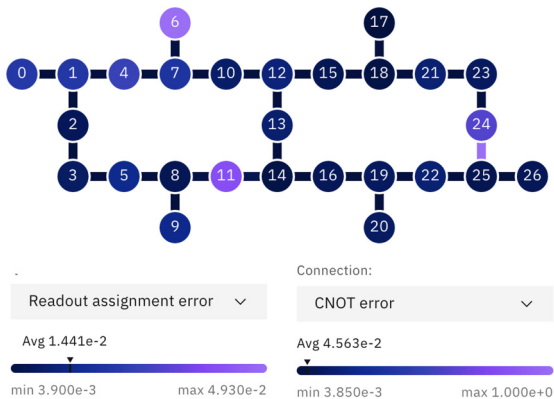

FIG. 6. Topology of the superconducting quantum device ibmq_kolkata with color map representation. Color associated to each qubit represents the readout error at the time of calibration while the color of the connection between two qubits represents the CNOT error rate. Image taken from the IBM Q Lab [83].

simulations are performed using a state vector and superimposed to exact diagonalization. For $\gamma = 0.67$, VQE seems at first to fail in computing the third excited state but actually finds degenerate states. To better understand the degeneracy, let us consider $\gamma = 1$ and use Eq. (8) to obtain

$$H|j, m\rangle = \left[-\tfrac{1}{2}(j(j+1) - m^2 - 2) - 2Bm \right]|j, m\rangle. \quad (11)$$

For $N = 4$ spins, $j = 0, 1, 2$, leading to nine distinct degenerate values for the energies of the 16 eigenstates. The first degenerate eigenvalue for $B < \tfrac{1}{4}$ is the one with the $j = 1$, $m = 1$ quantum numbers. However, it becomes the fourth excited for $\tfrac{1}{4} < B < \tfrac{1}{2}$, the third for $\tfrac{1}{2} < B < \tfrac{5}{4}$, and, finally, the second for B greater than $\tfrac{5}{4}$. Numerical investigations suggest an analogous behavior for $\gamma \neq 1$ and $0 < \gamma \lesssim 2$. In the region $B \lesssim \tfrac{5}{4}\sqrt{\gamma}$, the first eigenvalue to be degenerate is the third excited while in $B \gtrsim \tfrac{5}{4}\sqrt{\gamma}$, it is the second excited. Hence, VQE actually shows in Fig. 9 that for $B \approx 1.2$, the third eigenvalue is degenerate (3 times, in particular). The numerical investigations for $\gamma = 1$ show that the degenerate levels are

(i) threefold: $j = 1$, $m \in \{0, \pm 1\}$,
(ii) twofold: $j = 0$, $m = 0$,

in agreement with Ref. [77]. A similar argument can be addressed also to justify the behavior of the energies of the excited states for the model with $\gamma \neq 1$ as those observed in Fig. 9. However, the impossibility to diagonalize the two terms of the Hamiltonian in a common basis would make the argument only less intuitive and more cumbersome.

V. DISCUSSION AND OUTLOOKS

The advent of reliable quantum hardware, although not yet fault tolerant, has paved the way to novel techniques to tackle problems from different research areas. A natural avenue of research is the one that incorporates the quantum computing techniques to understand the physics of complex systems as many-body systems. To this end, we have proposed a way to exploit the variational quantum eigensolver, and the algorithms stemmed from it to study the finite-size criticality of paradigmatic spin models. On introducing a Hamiltonian
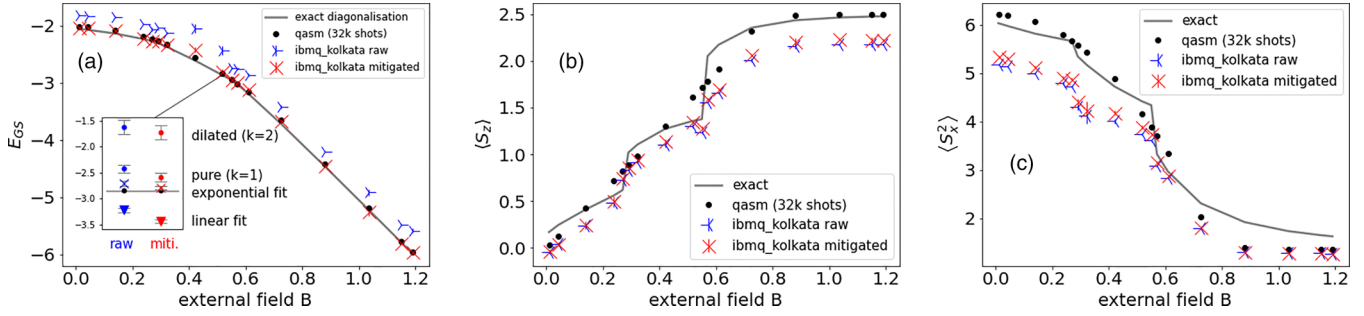
FIG. 7. We report the three relevant quantities to detect the criticality in a fully connected spin system, using the VQE algorithm run on the superconducting device ibmq_kolkata. The energy gap $E_{1st} - E_{GS}$ is in (a). The mean value of two magnetic observables: In (b) the correlation function along an axis transverse to the magnetic field $\langle S_x^2 \rangle$, and in (c) the mean magnetization along the direction of the magnetic field $\langle S_z \rangle$. The results are done for a lattice size of $N = 5$ spins at $\gamma = 0.49$. Points are obtained on the superconducting device ibmq_kolkata with (red crosses) and without (blue tri-left markers) error mitigation. The experimental values are compared to noiseless simulation (black dots) and the final benchmark is given by the exact diagonalization values (solid line). The inset in (a) shows the extrapolation to the zero noise regime, both with an exponential and linear fit.

with an anisotropic interaction γ in the x-y plane we have studied the level crossings between the ground-state and the first excited state in the proper LMG ($0 < \gamma < 1$) and in the two limit cases: the fully connected Ising model ($\gamma = 0$) and the Lipkin-Dicke model $\gamma = 1$. We used as a figure of merit some relevant magnetic observables, i.e., the magnetization along the field direction and the spin-spin correlation along the x axis.

Due to the geometry of the system, no length scale of the correlation can be defined, and this makes the fully connected spin models interesting systems to look for unconventional results at finite size [65,80] or to give a quantitative evaluation of the quality of a new computational or experimental technique [66,70,76].

Looking at this LMG model the number of measurements scale maximally at three for the three independent terms in the

Hamiltonian that do not commute. According to the results presented so far, it turns out that a limiting factor in getting better performance is the noise while the barren plateau represents potentially a second-order factor.

Recently, several papers [33–36] addressed the Lipkin model on a quantum computer to question whether techniques and methods proper of quantum machine learning can be employed in nuclear physics. In general, the authors rely on a system size of relatively small dimensions $N \leqslant 4$ to perform a preliminary noiseless analysis for the isotropic model that can be analytically solved exactly.
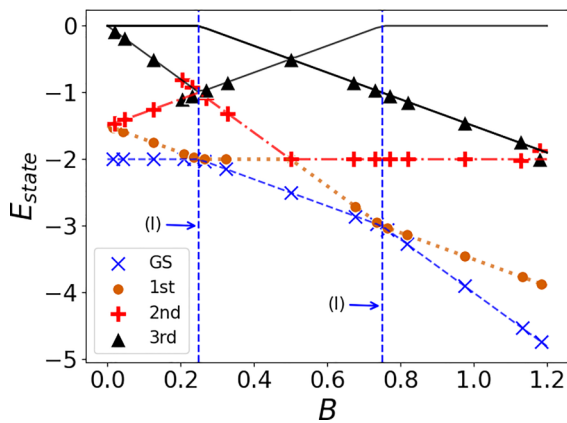

FIG. 8. Representation of various excited states for $N = 4$ and $\gamma = 1$. VQE results are represented by a blue cross (ground state), an orange dot (first excited state), a red plus (second excited state), and a black triangle (third excited state). The blue dashed line (ground state), the orange dotted line (first excited state), the red dot-dashed line (second excited state), and the black solid lines (third, fourth, fifth, and sixth excited states, some are degenerate) represent the classical diagonalization values. Vertical lines indicate crossing points.
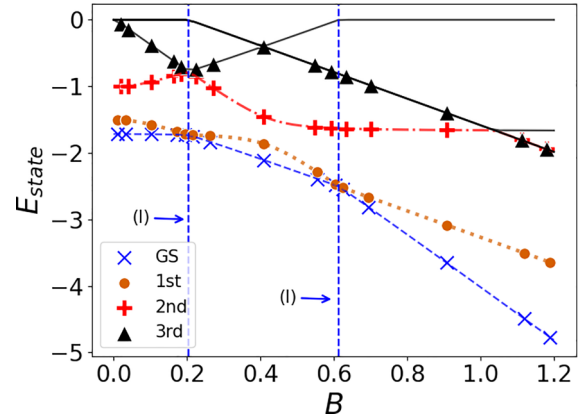

FIG. 9. We plot the energies E_{2nd} and E_{3rd} of the two excited states, beyond the first one, for the Hamiltonian in Eq. (7) with $N = 4$ at the value anisotropy $\gamma = 0.67$. In order to make the comparison clear, we report also the values of the energies of the ground state E_{GS} and of the first one E_{1st}. The markers of the VQE results are the following: blue cross for the ground-state energy, an orange dot for the first excited state, a red plus for second excited state, and a black triangle for third excited state. Exact diagonalization results are shown as a blue dashed line (ground state), an orange dotted line (first excited state), and a red dot-dashed line (second excited state), while the black solid lines are for the energies of degenerated states (ranging from the third excited and up to the sixth). Vertical lines indicate crossing points [see Eq. (9)].
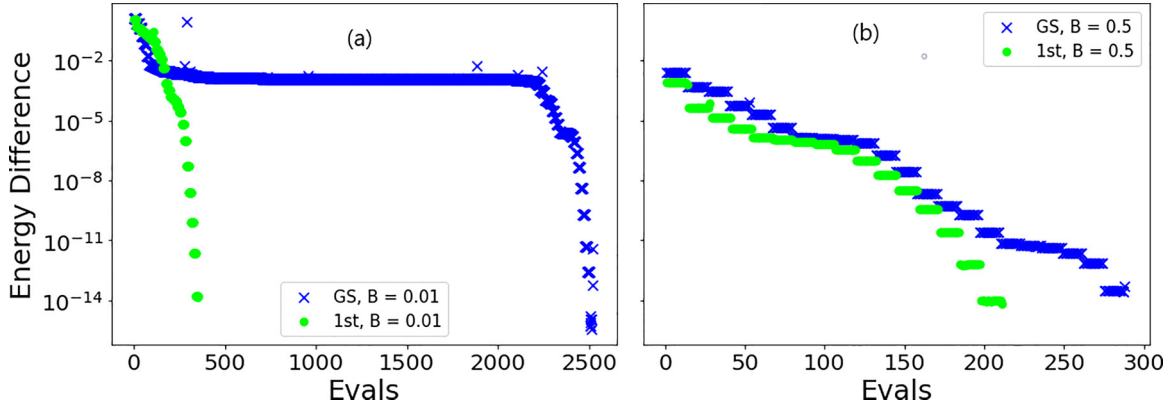
FIG. 10. We plot the SLSQP loss curve for the two lowest-energy states for different values of the magnetic field. Namely, in (a) we set $B = 0.01$ and in (b) $B = 0.5$ for $N = 4$ spins at $\gamma = 0.49$. The blue crosses refers to the ground state (GS) and the green filled circles to the first excited state (1st).

Our analysis is complementary to those previously carried out and goes in the direction of employing quantum algorithms to have a direct insight on problems of relevance in statistical physics. In fact, we have shown that the VQE is a powerful tool to assess the quantum phase transition of critical systems of finite size. We have also addressed how to mitigate the errors present when employing NISQ devices and how it is feasible on real hardware based on superconducting transmon qubits.

As final remark and open question, we surmise that our method could be employed in the future, when better-performing hardware with more qubits will be available as a benchmark for the renormalization group approaches used to study the finite-size scaling behavior of quantities of interest in statistical and condensed-matter theory.

APPENDIX: PERFORMANCE OF THE OPTIMIZER

In this section we give additional information and further explanation about the techniques adopted in this work. The gate-based quantum circuits used in this work are built using the open-source framework `qiskit-nature` [90].

The *state vector simulation* results are referred to classical simulation of a quantum circuit, probing the potential of this approach under ideal conditions, such as using exponentially many shots, without noise. For the optimization in a state vector setting we use Sequential Least SQuares Programming (SLSQP) [81]. It minimizes a function of several variables with any combination of bounds and equality and inequality constraints. We refer to scipy for further details.

We have termed QASM simulations the results obtained via the noise free simulation of the quantum circuit and the measurements and for which a finite statistics has been collected. This implies the simulation of probability outcomes of quantum observable given as a sequence of bit strings with the relative counts or number of repetitions. For the optimization in a state vector setting we use COBYLA [82]. This is a gradient-free optimizer like the one used for optimization on the quantum computer: the SPSA [86] optimizer. Differently from gradient based optimization, where the next best parameters in the optimization are obtained from the gradient of a given function with a high possibility to be stuck in a local minima/maxima when traversing parameter(s), SPSA efficiently approximates the gradient with few circuit evaluations by shifting the parameters in two random directions. The learning rate is changed at every bunch of iterations to ensure a fast convergence at the beginning and avoid oscillations at the end. Looking at realistic experiments, the stochastic nature of SPSA makes it resilient to the statistical noise coming from the finite number of measurements, making it appealing for quantum devices. A quantum natural variant of the SPSA optimizer using the geometry of the Hilbert space has been recently proposed by Gacon *et al.* [91]. In this variant the Hessian is approximated with six circuit evaluations and significantly improves the optimization efficiency of quantum circuits. In the present work, this optimizer is not considered.

To better understand the performance and the behavior of the optimizer we provide the loss curve during the learning process for the SLSQP (state vector simulation) optimizer in Fig. 10. The energy difference in the plot is given by:

$$\log \frac{E_{\mathrm{count}} - E_{\mathrm{final}}}{E_{\mathrm{final}}}. \tag{A1}$$

The huge difference in the number of evaluations needed between the first B value and $B = 0.5$ shows one of the benefits of taking the last B value optimal parameters as the initial ones for the next B.

[1] J. Zinn-Justin, *Phase Transitions and Renormalization Group* (Oxford University Press on Demand, New York, 2007).

[2] A. Pelissetto and E. Vicari, Critical phenomena and renormalization-group theory, Phys. Rep. **368**, 549 (2002).

[3] F. Englert and R. Brout, Broken symmetry and the mass of gauge vector mesons, Phys. Rev. Lett. **13**, 321 (1964).

[4] P. W. Higgs, Broken symmetries and the masses of gauge bosons, Phys. Rev. Lett. **13**, 508 (1964).

[5] J. Bardeen, L. N. Cooper, and J. R. Schrieffer, Theory of superconductivity, Phys. Rev. **108**, 1175 (1957).

[6] D. R. Tilley and J. Tilley, *Superfluidity and superconductivity* (Routledge, Abdingdom-on-Thames, UK, 2019).

[7] L. Amico, R. Fazio, A. Osterloh, and V. Vedral, Entanglement in many-body systems, Rev. Mod. Phys. **80**, 517 (2008).

[8] F. Schäfer, T. Fukuhara, S. Sugawa, Y. Takasu, and Y. Takahashi, Tools for quantum simulation with ultracold atoms in optical lattices, Nat. Rev. Phys. **2**, 411 (2020).

[9] S. Sachdev, *Quantum Phase Transitions*, 2nd ed. (Cambridge University Press, 2011).

[10] S. L. Sondhi, S. M. Girvin, J. P. Carini, and D. Shahar, Continuous quantum phase transitions, Rev. Mod. Phys. **69**, 315 (1997).

[11] M. E. Fisher and M. N. Barber, Scaling theory for finite-size effects in the critical region, Phys. Rev. Lett. **28**, 1516 (1972).

[12] E Brézin and J. Zinn-Justin, Finite size effects in phase transitions, Nucl. Phys. B **257**, 867 (1985).

[13] A. Osterloh, L. Amico, G. Falci, and R. Fazio, Scaling of entanglement close to a quantum phase transition, Nature (London) **416**, 608 (2002).

[14] Z. Zhu, G. Sun, W.-L. You, and D.-N. Shi, Fidelity and criticality of a quantum ising chain with long-range interactions, Phys. Rev. A **98**, 023607 (2018).

[15] M.-J. Hwang and M. B. Plenio, Quantum phase transition in the finite Jaynes-Cummings lattice systems, Phys. Rev. Lett. **117**, 123602 (2016).

[16] R. Botet and R. Jullien, Large-size critical behavior of infinitely coordinated systems, Phys. Rev. B **28**, 3955 (1983).

[17] I. Cong, S. Choi, and M. D. Lukin, Quantum convolutional neural networks, Nat. Phys. **15**, 1273 (2019).

[18] J. Herrmann, S. M. Llima, A. Remm, P. Zapletal, N. A. McMahon, C. Scarato, F. Swiadek, C. K. Andersen, C. Hellings, S. Krinner, N. Lacroix, S. Lazar, M. Kerschbaum, D. C. Zanuz, G. J. Norris, M. J. Hartmann, A. Wallraff, and C. Eichler, Realizing quantum convolutional neural networks on a superconducting quantum processor to recognize quantum phases, Nat. Commun. **13**, 4144 (2022).

[19] S. Monaco, O. Kiss, A. Mandarino, S. Vallecorsa, and M. Grossi, Quantum phase detection generalization from marginal quantum neural network models, Phys. Rev. B **107**, L081105 (2023).

[20] K. Kottmann, F. Metz, J. Fraxanet, and N. Baldelli, Variational quantum anomaly detection: Unsupervised mapping of phase diagrams on a physical quantum computer, Phys. Rev. Res. **3**, 043184 (2021).

[21] J. Gibbs, Z. Holmes, M. C. Caro, N. Ezzell, H.-Y. Huang, L. Cincio, A. T. Sornborger, and P. J. Coles, Dynamical simulation via quantum machine learning with provable generalization, arXiv:2204.10269.

[22] A. Daley, I. Bloch, C. Kokail, S. Flannigan, N. Pearson, M. Troyer, and P. Zoller, Practical quantum advantage in quantum simulation, Nature (London) **607**, 667 (2022).

[23] H. J. Lipkin, N. Meshkov, and A. Glick, Validity of many-body approximation methods for a solvable model: (I). Exact solutions and perturbation theory, Nucl. Phys. **62**, 188 (1965).

[24] N. Meshkov, A. Glick, and H. Lipkin, Validity of many-body approximation methods for a solvable model: (II). Linearization procedures, Nucl. Phys. **62**, 199 (1965).

[25] A. Glick, H. Lipkin, and N. Meshkov, Validity of many-body approximation methods for a solvable model: (III). Diagram summations, Nucl. Phys. **62**, 211 (1965).

[26] J. Preskill, Quantum computing in the NISQ era and beyond, Quantum **2**, 79 (2018).

[27] K. Bharti, A. Cervera-Lierta, T. H. Kyaw, T. Haug, S. Alperin-Lea, A. Anand, M. Degroote, H. Heimonen, J. S. Kottmann, T. Menke, W.-K. Mok, S. Sim, L.-C. Kwek, and A. Aspuru-Guzik, Noisy intermediate-scale quantum algorithms, Rev. Mod. Phys. **94**, 015004 (2022).

[28] A. Uvarov, J. D. Biamonte, and D. Yudin, Variational quantum eigensolver for frustrated quantum systems, Phys. Rev. B **102**, 075104 (2020).

[29] O. Castaños, R. López-Peña, J. G. Hirsch, and E. López-Moreno, Phase transitions and accidental degeneracy in nonlinear spin systems, Phys. Rev. B **72**, 012406 (2005).

[30] H.-M. Kwok, W.-Q. Ning, S.-J. Gu, and H.-Q. Lin, Quantum criticality of the Lipkin-Meshkov-Glick model in terms of fidelity susceptibility, Phys. Rev. E **78**, 032103 (2008).

[31] J. Ma, X. Wang, and S.-J. Gu, Many-body reduced fidelity susceptibility in Lipkin-Meshkov-Glick model, Phys. Rev. E **80**, 021124 (2009).

[32] D. Gonzalez, D. Gutiérrez-Ruiz, and J. D. Vergara, Classical description of the parameter space geometry in the Dicke and Lipkin-Meshkov-Glick models, Phys. Rev. E **104**, 014113 (2021).

[33] M. J. Cervia, A. B. Balantekin, S. N. Coppersmith, C. W. Johnson, P. J. Love, C. Poole, K. Robbins, and M. Saffman, Lipkin model on a quantum computer, Phys. Rev. C **104**, 024305 (2021).

[34] K. Robbins and P. J. Love, Benchmarking near-term quantum devices with the variational quantum eigensolver and the Lipkin-Meshkov-Glick model, Phys. Rev. A **104**, 022412 (2021).

[35] A. Chikaoka and H. Liang, Quantum computing for the lipkin model with unitary coupled cluster and structure learning ansatz, Chin. Phys. C **46**, 024106 (2022).

[36] A. M. Romero, J. Engel, H. L. Tang, and S. E. Economou, Solving nuclear structure problems with the adaptive variational quantum algorithm, Phys. Rev. C **105**, 064317 (2022).

[37] A. Peruzzo, J. McClean, P. Shadbolt, M.-H. Yung, X.-Q. Zhou, P. J. Love, A. Aspuru-Guzik, and J. L. O'Brien, A variational eigenvalue solver on a photonic quantum processor, Nat. Commun. **5**, 4213 (2014).

[38] J. Tilly, H. Chen, S. Cao, D. Picozzi, K. Setia, Y. Li, E. Grant, L. Wossnig, I. Rungger, G. H. Booth *et al.*, The variational quantum eigensolver: A review of methods and best practices, Phys. Rep. **986**, 1 (2022).

[39] J. R. McClean, J. Romero, R. Babbush, and A. Aspuru-Guzik, The theory of variational hybrid quantum-classical algorithms, New J. Phys. **18**, 023023 (2016).

[40] J. Romero, R. Babbush, J. R. McClean, C. Hempel, P. J. Love, and A. Aspuru-Guzik, Strategies for quantum computing

molecular energies using the unitary coupled cluster ansatz, Quantum Sci. Technol. **4**, 014008 (2019).

[41] A. Kandala, A. Mezzacapo, K. Temme, M. Takita, M. Brink, J. M. Chow, and J. M. Gambetta, Hardware-efficient variational quantum eigensolver for small molecules and quantum magnets, Nature (London) **549**, 242 (2017).

[42] L. Crippa, F. Tacchino, M. Chizzini, A. Aita, M. Grossi, A. Chiesa, P. Santini, I. Tavernelli, and S. Carretta, Simulating static and dynamic properties of magnetic molecules with prototype quantum computers, Magnetochemistry **7**, 117 (2021).

[43] P. K. Barkoutsos, J. F. Gonthier, I. Sokolov, N. Moll, G. Salis, A. Fuhrer, M. Ganzhorn, D. J. Egger, M. Troyer, A. Mezzacapo, S. Filipp, and I. Tavernelli, Quantum algorithms for electronic structure calculations: Particle-hole hamiltonian and optimized wave-function expansions, Phys. Rev. A **98**, 022322 (2018).

[44] E. F. Dumitrescu, A. J. McCaskey, G. Hagen, G. R. Jansen, T. D. Morris, T. Papenbrock, R. C. Pooser, D. J. Dean, and P. Lougovski, Cloud Quantum Computing of an Atomic Nucleus, Phys. Rev. Lett. **120**, 210501 (2018).

[45] I. Stetcu, A. Baroni, and J. Carlson, Variational approaches to constructing the many-body nuclear ground state for quantum computing, Phys. Rev. C **105**, 064308 (2022).

[46] O. Kiss, M. Grossi, P. Lougovski, F. Sanchez, S. Vallecorsa, and T. Papenbrock, Quantum computing of the ^{6}Li nucleus via ordered unitary coupled clusters, Phys. Rev. C **106**, 034325 (2022).

[47] M. Dupont and J. E. Moore, Quantum criticality using a superconducting quantum processor, Phys. Rev. B **106**, L041109 (2022).

[48] M. Q. Hlatshwayo, Y. Zhang, H. Wibowo, R. LaRose, D. Lacroix, and E. Litvinova, Simulating excited states of the lipkin model on a quantum computer, Phys. Rev. C **106**, 024319 (2022).

[49] M. Benedetti, E. Lloyd, S. Sack, and M. Fiorentini, Parameterized quantum circuits as machine learning models, Quant. Sci. Technol. **4**, 043001 (2019).

[50] A. Anand, P. Schleich, S. Alperin-Lea, P. W. K. Jensen, S. Sim, M. Díaz-Tinoco, J. S. Kottmann, M. Degroote, A. F. Izmaylov, and A. Aspuru-Guzik, A quantum computing view on unitary coupled cluster theory, Chem. Soc. Rev. **51**, 1659 (2022).

[51] J. Lee, W. J. Huggins, M. Head-Gordon, and K. B. Whaley, Generalized unitary coupled cluster wave functions for quantum computation, J. Chem. Theory Comput. **15**, 311 (2019).

[52] J. R. McClean, S. Boixo, V. N. Smelyanskiy, R. Babbush, and H. Neven, Barren plateaus in quantum neural network training landscapes, Nat. Commun. **9**, 4812 (2018).

[53] L. Schatzki, M. Larocca, Q. T. Nguyen, F. Sauvage, and M. Cerezo, Theoretical guarantees for permutation-equivariant quantum neural networks, arXiv:2210.09974.

[54] H. R. Grimsley, S. E. Economou, E. Barnes, and N. J. Mayhall, An adaptive variational algorithm for exact molecular simulations on a quantum computer, Nat. Commun. **10**, 3007 (2019).

[55] O. Higgott, D. Wang, and S. Brierley, Variational quantum computation of excited states, Quantum **3**, 156 (2019).

[56] P. J. Ollitrault, A. Kandala, C.-F. Chen, P. K. Barkoutsos, A. Mezzacapo, M. Pistoia, S. Sheldon, S. Woerner, J. M. Gambetta, and I. Tavernelli, Quantum equation of motion for computing molecular excitation energies on a noisy quantum processor, Phys. Rev. Res. **2**, 043140 (2020).

[57] J. Tilly, G. Jones, H. Chen, L. Wossnig, and E. Grant, Computation of molecular excited states on IBM quantum computers using a discriminative variational quantum eigensolver, Phys. Rev. A **102**, 062425 (2020).

[58] K. M. Nakanishi, K. Mitarai, and K. Fujii, Subspace-search variational quantum eigensolver for excited states, Phys. Rev. Res. **1**, 033062 (2019).

[59] P. D. Nation, H. Kang, N. Sundaresan, and J. M. Gambetta, Scalable mitigation of measurement errors on quantum computers, PRX Quant. **2**, 040326 (2021).

[60] A. He, B. Nachman, W. A. de Jong, and C. W. Bauer, Zero-noise extrapolation for quantum-gate error mitigation with identity insertions, Phys. Rev. A **102**, 012426 (2020).

[61] A. Kandala, K. Temme, A. D. Córcoles, A. Mezzacapo, J. M. Chow, and J. M. Gambetta, Error mitigation extends the computational reach of a noisy quantum processor, Nature (London) **567**, 491 (2019).

[62] L. F. Richardson, IX. The approximate arithmetical solution by finite differences of physical problems involving differential equations, with an application to the stresses in a masonry dam, Philos. Trans. Roy. Soc. Lond. Ser. A **210**, 307 (1911).

[63] R. Takagi, S. Endo, S. Minagawa, and M. Gu, Fundamental limits of quantum error mitigation, npj Quant. Inf. **8**, 114 (2022).

[64] E. Lieb, T. Schultz, and D. Mattis, Two soluble models of an antiferromagnetic chain, Ann. Phys. **16**, 407 (1961).

[65] S. Dusuel and J. Vidal, Continuous unitary transformations and finite-size scaling exponents in the Lipkin-Meshkov-Glick model, Phys. Rev. B **71**, 224420 (2005).

[66] J. I. Cirac, M. Lewenstein, K. Mølmer, and P. Zoller, Quantum superposition states of Bose-Einstein condensates, Phys. Rev. A **57**, 1208 (1998).

[67] D. A. Garanin, X. Martínez Hidalgo, and E. M. Chudnovsky, Quantum-classical transition of the escape rate of a uniaxial spin system in an arbitrarily directed field, Phys. Rev. B **57**, 13639 (1998).

[68] O. Castaños, R. López-Peña, J. G. Hirsch, and E. López-Moreno, Classical and quantum phase transitions in the Lipkin-Meshkov-Glick model, Phys. Rev. B **74**, 104118 (2006).

[69] J. Ma and X. Wang, Fisher information and spin squeezing in the Lipkin-Meshkov-Glick model, Phys. Rev. A **80**, 012318 (2009).

[70] J. Vidal, G. Palacios, and C. Aslangul, Entanglement dynamics in the Lipkin-Meshkov-Glick model, Phys. Rev. A **70**, 062304 (2004).

[71] S. Dusuel and J. Vidal, Finite-Size Scaling Exponents of the Lipkin-Meshkov-Glick Model, Phys. Rev. Lett. **93**, 237204 (2004).

[72] P. Ribeiro, J. Vidal, and R. Mosseri, Exact spectrum of the Lipkin-Meshkov-Glick model in the thermodynamic limit and finite-size corrections, Phys. Rev. E **78**, 021106 (2008).

[73] G. Salvatori, A. Mandarino, and M. G. A. Paris, Quantum metrology in Lipkin-Meshkov-Glick critical systems, Phys. Rev. A **90**, 022111 (2014).

[74] A. Mandarino, K. Joulain, M. D. Gómez, and B. Bellomo, Thermal transistor effect in quantum systems, Phys. Rev. Appl. **16**, 034026 (2021).

[75] A. Mandarino, Quantum thermal amplifiers with engineered dissipation, Entropy **24**, 1031 (2022).

[76] D Agassi, H. Lipkin, and N Meshkov, Validity of many-body approximation methods for a solvable model: (IV). The deformed Hartree-Fock solution, Nucl. Phys. **86**, 321 (1966).

[77] R. H. Dicke, Coherence in spontaneous radiation processes, Phys. Rev. **93**, 99 (1954).

[78] A. Das, K. Sengupta, D. Sen, and B. K. Chakrabarti, Infinite-range ising ferromagnet in a time-dependent transverse magnetic field: Quench and ac dynamics near the quantum critical point, Phys. Rev. B **74**, 144423 (2006).

[79] S. Lerma H. and J. Dukelsky, The Lipkin-Meshkov-Glick model as a particular limit of the su(1,1) Richardson-Gaudin integrable models, Nucl. Phys. B **870**, 421 (2013).

[80] G. Chen and J. Liang, Unconventional quantum phase transition in the finite-size Lipkin–Meshkov–Glick model, New J. Phys. **8**, 297 (2006).

[81] D. Kraft, *A Software Package for Sequential Quadratic Programming*, Deutsche Forschungs- und Versuchsanstalt für Luft- und Raumfahrt Köln: Forschungsbericht (Wiss. Berichtswesen d. DFVLR, 1988).

[82] S. M. Harwood, D. Trenev, S. T. Stober, P. Barkoutsos, T. P. Gujarati, S. Mostame, and D. Greenberg, Improving the variational quantum eigensolver using variational adiabatic quantum computing, ACM Trans. Quant. Comput. **3**, 1 (2022).

[83] https://quantum-computing.ibm.com/services/resources?system=ibmq_kolkata.

[84] J. M. Chow, A. D. Córcoles, J. M. Gambetta, C. Rigetti, B. R. Johnson, J. A. Smolin, J. R. Rozen, G. A. Keefe, M. B. Rothwell, M. B. Ketchen, and M. Steffen, Simple All-Microwave Entangling Gate for Fixed-Frequency Superconducting Qubits, Phys. Rev. Lett. **107**, 080502 (2011).

[85] G. Li, Y. Ding, and Y. Xie, Tackling the qubit mapping problem for nisq-era quantum devices, *Proceedings of the 24th International Conference on Architectural Support for Programming Languages and Operating Systems (ASPLOS '19)* (Association for Computing Machinery, New York, NY, 2019), pp. 1001–1014.

[86] J. C. Spall, Implementation of the simultaneous perturbation algorithm for stochastic optimization, IEEE Trans. Aerosp. Electron. Syst. **34**, 817 (1998).

[87] U. Schollwöck, The density-matrix renormalization group, Rev. Mod. Phys. **77**, 259 (2005).

[88] M. Schuld, V. Bergholm, C. Gogolin, J. Izaac, and N. Killoran, Evaluating analytic gradients on quantum hardware, Phys. Rev. A **99**, 032331 (2019).

[89] S. Endo, S. C. Benjamin, and Y. Li, Practical Quantum Error Mitigation for Near-Future Applications, Phys. Rev. X **8**, 031027 (2018).

[90] Md Sajid Anis *et al.*, Qiskit: An Open-Source Framework for Quantum Computing (2021), doi:10.5281/zenodo.2573505.

[91] J. Gacon, C. Zoufal, G. Carleo, and S. Woerner, Simultaneous perturbation stochastic approximation of the quantum Fisher information, Quantum **5**, 567 (2021).